

Terahertz s-SNOM reveals nanoscale conductivity of graphene

Henrik Bødker Lassen¹, Edmund John Railton Kelleher¹,
Leonid Iliushyn², Timothy J. Booth², Peter Bøggild²,
Peter Uhd Jepsen^{1*}

¹DTU Electro, Department of Electrical and Photonics Engineering,
Technical University of Denmark, Ørsteds Plads 343, Kongens Lyngby,
DK-2800, Denmark.

²DTU Physics, Department of Physics, Technical University of
Denmark, Fysikvej 311, Kongens Lyngby, DK-2800, Denmark.

*Corresponding author(s). E-mail(s): puje@dtu.dk;

Abstract

The nanoscale contrast in scattering-type scanning near-field optical microscopy (s-SNOM) is determined by the optical properties of the sample immediately under the apex of the tip of the atomic force microscope (AFM). There are several models that describe the optical scattering of an incident field by the tip near a surface, and these models have been successful in relating the measured scattering signal to the dielectric function of the sample under the tip. Here, we address a situation that is normally not considered in the existing interaction models, namely the near-field signal arising from thin, highly conductive films in the terahertz (THz) frequency range. According to established theoretical models, highly conductive thin films should show insignificant contrast in the THz range for small variations in conductivity, therefore hindering the use of s-SNOM for nanoscale characterisation. We experimentally demonstrate unexpected but clear and quantifiable layer contrast in the THz s-SNOM signal from few-layer exfoliated graphene as well as subtle nanoscale contrast variations within graphene layers. We use finite-element simulations to confirm that the observed contrast is described by the classical electromagnetics of the scattering mechanism, suggesting that the dipole models must be reformulated to correctly describe the interaction with conductive samples.

Keywords: s-SNOM, electrical conductivity, graphene, thin films, terahertz

1 Introduction

Characterization of the electrical properties of thin-film materials is crucial for developing and producing electronic components, including high-quality integrated circuits, touch-sensitive screens, and solar panels. Optical methods offer the benefit of contactless techniques for non-invasive measurements. Far-field imaging at terahertz frequencies (0.1-30 THz) has proven to be a versatile contactless approach for the investigation of the optical conductivity of materials, and especially so for the full assessment of the electric properties of large-area graphene grown by chemical vapour deposition, providing spatially resolved maps of DC conductivity, carrier concentration, Fermi energy, and electron scattering time [1–4]. However, the diffraction limit prevents the investigation of smaller areas of graphene obtained by exfoliation.

Scattering-type scanning near-field optical microscopy (s-SNOM) is based on detecting variations of the scattering amplitude and phase of a light beam focused onto a sharp tip (a scanning AFM probe in modern implementations) that is brought into proximity with a sample. The technique has evolved dramatically since the initial demonstrations [5, 6]. The capability of deep sub-wavelength resolution virtually independent of wavelength [7], together with the invention of harmonic demodulation techniques for suppression of the dominant far-field contribution to the scattering signal [8, 9] have led to the commercialization and widespread use of s-SNOM in the mid-IR and near-IR regions. The technique is also a versatile tool for investigating the THz dynamics of materials on the nanoscale, including graphene and other 2D materials. The THz s-SNOM (THz-SNOM) has therefore become increasingly popular in recent years, implemented with both all-electronic sub-THz sources [10–13], more widely used THz laser sources (for example, Refs. 14, 15), THz radiation from a free-electron laser [16], and pulsed broadband THz sources known from THz time-domain spectroscopy [17] (THz-TDS) [18–24]. Despite this utility, in previous reports, it has been shown that THz-SNOM provides no useful contrast when investigating certain highly conductive materials: for example, rendering few-layer graphene as indistinguishable from monolayers [19, 25].

Here, we demonstrate that THz-SNOM is, despite these earlier reported results, in fact, a versatile tool for spatially resolving the conductivity of graphene at the nanoscale. We show a readily identifiable contrast that enables a clear distinction of the layer structure of exfoliated graphene flakes and local variation of the conductivity within monolayer graphene flakes. To date, there have been no proven methods for the assessment of conductivity on the nanoscale. Our demonstration of THz-SNOM for detecting subtle sub-micron variations in the conductivity of graphene, therefore, represents an important step-forward that is relevant across several disciplines. The nondestructive and contactless nature of the measurement allows the characterization of conductive 2D materials encapsulated in hexagonal boron nitride (hBN) and exotic materials such as twisted bilayers, where Moiré effects can also influence the local electronic properties. Other nanoscale probes cannot directly determine the conductivity. For instance, scanning tunneling microscopy (STM) measures the density of states of electrons in the surface of materials—not the conductivity.

2 Results and Discussion

2.1 State-of-the-art theoretical models

The most widely used theoretical descriptions of the interaction between the AFM tip and the sample are the Point Dipole Model (PDM) [9, 26], the Finite Dipole Model (FDM) [27], and the Lightning Rod Model (LRM) [28]. These are self-consistent, quasi-electrostatic models that predict the scattering of a low-frequency (no retardation effects) optical field from the AFM tip. The scattered field from the illuminated tip is determined in all models as $E_{\text{sca}} = \alpha_{\text{eff}}(1 + r_p^2)E_{\text{inc}}$ where α_{eff} is the effective polarisability of the tip-sample system and r_p is the far-field reflection coefficient of the sample. This reflection is often ignored in SNOM measurements when it can be justified that it varies insignificantly across the scanned area, or is removed by normalization procedures [29]. The PDM models the AFM tip as a point dipole and thus offers no predictions regarding the influence of the tip shape. Despite this apparent limitation, the PDM has been successful in a qualitative explanation of the s-SNOM response of dielectric samples in the mid-infrared (MIR) spectral region [30, 31]. The FDM was developed to address some of the shortcomings of the PDM by modelling the AFM tip as an elongated spheroidal shape and has been shown to give better quantitative agreement with the experimental results in the MIR than the PDM [27, 32].

Figure 1a shows a schematic illustration of the geometry of a tip modelled in the FDM. The FDM describes the effective polarisability of the tip-sample system as

$$\alpha_{\text{eff}}(t) \propto 1 + \frac{1}{2} \frac{\beta(\omega, q) f_0(t)}{1 - \beta(\omega, q) f_i(t)}, \quad (1)$$

where $f_0(t)$ and $f_i(t)$ are functions defined by the geometric parameters of the tip and the distance $h(t)$ between the tip apex and the sample surface (see Supplementary Information). The quasi-electrostatic reflection coefficient $\beta(\omega, q)$ holds the information about the optical properties (permittivity, conductivity) of the sample, evaluated at an in-plane momentum q of the electric near-field below the tip. Thin-film samples can be treated by the PDM and FDM by direct inclusion of the layered structure in the model [33] or by a modification of β to its thin-film equivalent [34].

The tip is tapped harmonically at a frequency Ω , with a tapping amplitude A and minimum distance h_0 , such that the height $h(t) = h_0 + \frac{1}{2}A(1 + \cos \Omega t)$. The scattered signal is detected as a function of time during the tapping cycle. Due to the non-linear relationship between the scattering signal and the tapping height, the detected signal contains overtones of the tapping frequency, and these overtones contain information about the amplitude and phase of the near-field [8, 9]. A frequency decomposition of the scattered signal yields the amplitude and phase of the signal S_m at the harmonic orders m of the tapping frequency, leading to strong suppression of far-field information. Hence, a spectroscopic measurement involves the recording of the scattered signal $E_{\text{sca}}(t)$ as a function of the tapping time, the decomposition into its harmonic orders, and finally, the inversion of either Eq. (1) or possibly a numerical model for the interaction to determine β and thus the permittivity or conductivity of the sample region under the tip. In time-domain THz-SNOM, a complete THz waveform is recorded as

a function of delay time τ so that the scattered signal E_{sca} is known for all frequencies within the bandwidth of the THz signal after its Fourier transformation.

If the sample consists of a bulk conductor or a thin, highly conductive film on top of a dielectric substrate, the FDM predicts that the scattered signal is insensitive to variations in the conductivity of the thin film. This is due to the high value of the dominant in-plane momentum ($q \sim 1/R$) of the light in the near-field zone under the tip, where R is the apex radius of the tip. At high in-plane momenta, the quasi-static reflection coefficient is very close to unity, and the scattered signal becomes only very weakly dependent on the specific sheet conductance of the thin film, irrespective of the nature of the conductivity [19] (see Supplementary Information for further details). Figure 1b illustrates the lack of contrast in the PDM and FDM at 1 THz for the ratio of the scattered signal from graphene and from a substrate (90 nm SiO₂ on Si), with the parameters $R = 50$ nm, $L = 600$ nm, $g = 0.7$, $q = 14.2 \mu\text{m}^{-1}$, and $A = 100$ nm. Both models predict a nearly constant scattering ratio across the 0.1 - 3 mS range of surface conductivity relevant for exfoliated and CVD-grown graphene under typical ambient conditions (indicated by the grey box in Fig. 1b).

Unsurprisingly, there has been serious doubt as to the usefulness of THz-SNOM with respect to imaging of highly conductive, technologically relevant materials at the nanoscale due to the lack of sensitivity of the widely used dipole models to the precise value of the surface conductivity. This predicted insensitivity has been confirmed in experimental THz-SNOM on multilayer exfoliated graphene flakes [19, 25] where no discernible contrast between the different layer thicknesses of graphene could be found: moreover, it was shown that the scattered signal from graphene for all layer combinations was comparable to a 30-nm thick gold film [19]. A similar conclusion was drawn in later experiments [25]. On the other hand, the scattering contrast between monolayer and few-layer WTe₂ buried under hexagonal boron nitride (hBN) was observed and found to be compatible with the LRM [23]. THz-SNOM at sub-THz frequency has also shown a high sensitivity to the local conductivity of CsPbBr₃ perovskite-grained films [13], and this contrast was found to be consistent with the FDM. As can be seen in Fig. 1b, the calculated contrast varies significantly with conductivity in both the PDM and the FDM for surface conductivities lower than 0.1 mS. The experimental results in these studies were obtained on samples with surface conductivities in this lower range, both for WTe₂ (0.01-0.1 mS) [23, 35] and CsPbBr₃ (0.05 mS) [13].

Here we present new results that demonstrate that it is indeed possible, and should even be expected, that THz-SNOM of exfoliated graphene yields good contrast between different numbers of graphene layers and also clearly visible contrast variation within single-layer graphene samples. The results show that the currently available theoretical models of s-SNOM measurements of conductive films fail to describe this observable contrast. Specifically, the finite dipole model and other electrostatic dipole models cannot directly describe the observations. This limitation of the FDM has been noted on earlier occasions by Kim *et al.* [36] who pointed out that a fully retarded tip-sample interaction would be required for the modelling of the s-SNOM signal from conductive samples. Here, we used finite-element (FEM) simulations to verify that the experimentally observed contrast can be reproduced in a simplified electromagnetic simulation that only accounts for electromagnetic interaction between an ideal

tip shape and the sample. Finally, we compare frequency-resolved spectroscopic THz-SNOM and corresponding FEM simulations that reveal that interference present in the experimental data is most likely due to standing waves on the AFM tip and its shaft, which must be considered before quantitative spectroscopy is possible in THz-SNOM.

2.2 Experimental details

We perform THz-SNOM with a commercial s-SNOM system (Attocube THz-NeaSCOPE) equipped with an integrated THz time-domain spectroscopy module (Attocube/Menlo Systems TeraSmart), as described in the Methods section. A schematic of the AFM tip over a sample with incident and scattered THz radiation is shown in Fig. 1a. In our 2D finite-element modelling (FEM) of the interaction presented in the following, we represent the scattered THz signal as the integrated y -component of the electric field on the surface of the AFM tip, as indicated in Fig. 1a [37].

The THz-SNOM signal is recorded with the AFM operating in tapping mode. We use demodulation of the real-time, periodic scattering signal and detect the overtones S_m of the tapping frequency Ω to suppress the dominant far-field background signal. We use the $m = 3$ overtone in the results presented below. A time trace of a scattered THz signal is represented by $S_m(\tau)$, where τ is the time delay along the THz time axis. Figure 1c shows representative THz transients $S_3(\tau)$ recorded on the substrate (blue curve) and on a graphene flake (orange curve), in this example displaying a contrast of approximately 2. The frequency spectra of the two signals are shown in Fig. 1d in the range 0.5 to 1.6 THz. We observe significant interference in the time traces and spectral shapes, most likely originating from a standing wave pattern on the AFM tip and shank [38, 39].

A full THz-SNOM imaging measurement requires recording the scattered signal at each position on a sample surface. In this case, full spectroscopic characterization of the surface across the spectral range of the system is possible. This can be a rather time-consuming procedure, so we perform what are known as white-light scans. This scan mode is implemented by operating the instrument at a delay time equivalent to the peak of the THz waveform, indicated by the arrow in Fig. 1c, while performing the surface scan. In this manner, the recorded image contains information on the average optical properties of the sample, weighted by the spectral amplitude of the THz signal across its bandwidth instead of a frequency-resolved image. For conductive samples, the optical conductivity across the low THz range ($\nu < 1/(2\pi\tau)$ where τ is the carrier scattering time) is not expected to change dramatically. Hence, a white-light scan acts as a frequency-averaged result that is a versatile two-dimensional representation of a full, three-dimensional hyperspectral data set.

A stronger scattering signal indicates a higher conductivity of the surface. Thus, imaging of a conductive surface with THz-SNOM gives information about the local optical conductivity in the THz range, with a resolution related to the radius of curvature of the AFM tip in use [40]. An indication of the resolution is shown in Fig. 1e, where the approach curves recorded at a position on a graphene flake are shown for the first four demodulation orders ($m = 1 - 4$). The decay length of the signals is 25, 15, and 10 nm for $m = 2, 3, 4$, respectively.

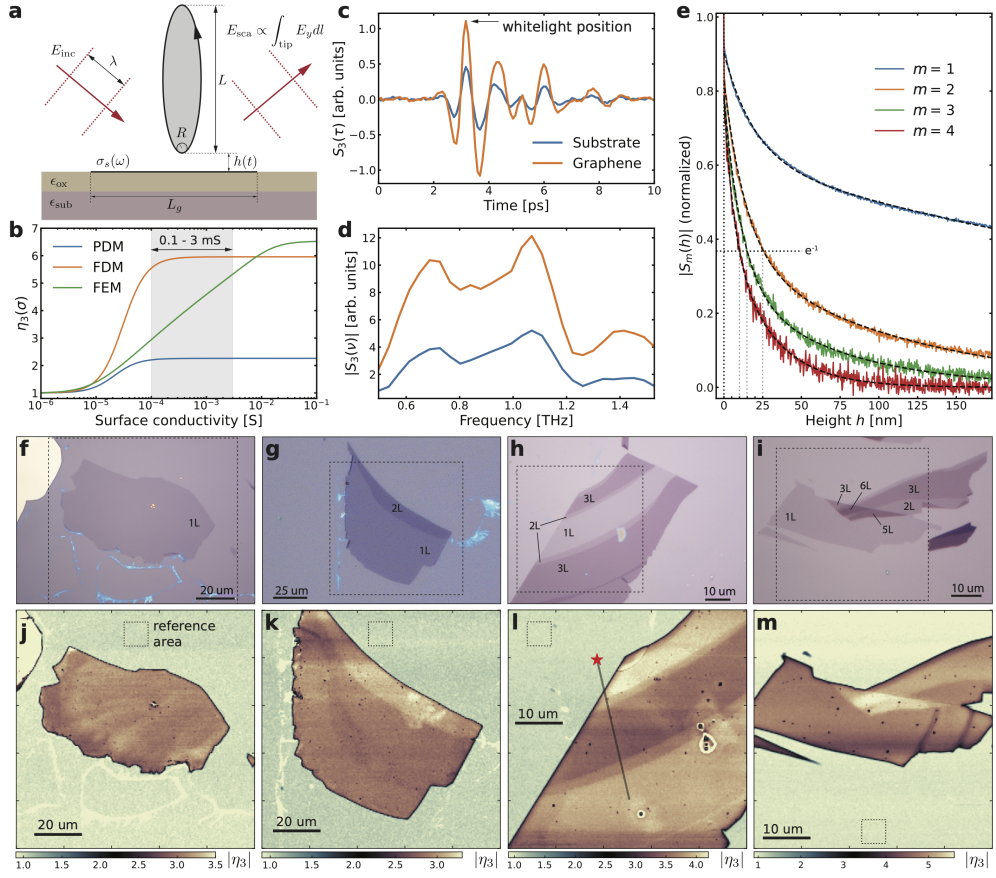


Fig. 1 (a) Schematic of considered THz-SNOM model. The ellipsoidal tip scatters an incoming THz field with a signal strength that depends on the distance from the layered sample and the properties of the sample. In our simulations, the scattered signal is represented as the integral of the electric field over the tip surface. (b) Typical contrast predictions of the PDM and FDM and finite element (FEM) simulations of the scattering signal relative to that of the substrate in THz-SNOM, as a function of sheet conductivity σ_s at a frequency of 1 THz. (c) Representative experimental THz-SNOM time-domain signals from the substrate and graphene. The horizontal arrow indicates the position of the time delay when recording white-light scans. (d) Spectral content of the scattered signals from substrate and graphene. (e) Representative approach curves for modulation orders $m = 1 - 4$ on graphene. The horizontal dotted line indicates the e^{-1} -level of the signals, indicative of the spatial resolution of the measurement. (f-i) Optical microscope images and (j-m) THz-SNOM white-light images of four different exfoliated graphene samples transferred to a SiO_2/Si substrate. The dashed boxes on the microscope images indicate the area scanned by THz-SNOM. The dashed boxes in the THz-SNOM images indicate the regions used to calculate the average signal from the substrate in normalization of the signal strength. The star and grey line in panel l indicate the start and path of a full frequency-resolved line scan. The THz-SNOM images show the scattering ratio $|\eta_3|$ at the third harmonic of the tapping frequency.

2.3 THz-SNOM on exfoliated graphene

Graphene samples were prepared as described in the Methods section. Exfoliated single-layer graphene on a standard SiO₂/Si substrate under ambient conditions typically displays a carrier concentration of $n \approx 10^{12} \text{ cm}^{-2}$ and a mobility $\mu \approx 3000 - 5000 \text{ cm}^2/\text{Vs}$. This carrier concentration corresponds to a Fermi energy of $\mathcal{E}_F \approx 0.12 \text{ eV}$ and the mobility corresponds to a carrier scattering time of $\tau \approx 33 - 55 \text{ fs}$, a mean free path of $\lambda_{\text{mf}} \approx 33 - 55 \text{ nm}$, and a DC conductivity $\sigma_{\text{dc}} \approx 0.42 - 0.71 \text{ mS}$ [41, 42].

Figures 1f-i (middle row) show optical microscope images of the graphene samples investigated here. Figures 1j-m (bottom row) show the corresponding THz-SNOM white-light images, represented by the magnitude of the third harmonic $|S_3|$ of the tapping signal relative to that obtained over a reference area on the substrate, indicated by the black, dashed squares in each image.

Figures 1f,j show a monolayer (1L) graphene flake extending in an irregular shape that covers approximately $80 \times 50 \mu\text{m}^2$, as identified in the optical microscope image. In the THz-SNOM white-light image (Fig. 1j), we see a contrast ratio between graphene and substrate of approximately 3 and a small defect in the central region of the flake. Importantly, we see well-defined local variations of the THz-SNOM scattering signal within the flake, visually resembling weathered geographical formations on a cartographic landmass, which could be attributed to the fact that no steps (beyond those outlined in the Methods section) to clean or homogenise the graphene (for example, annealing) were taken.

Figures 1g,k show an example of a graphene sample with a large monolayer region and a smaller two-layer (2L) region in the upper part of the monolithic flake. The corresponding THz-SNOM image shows clearly identifiable 2L and 1L regions with a 5-10% contrast. Moreover, we also observe local variations of the signal within these 1L and 2L regions, respectively.

Figures 1h,l show another example of a multilayer sample structure, with 1L, 2L, and three-layer (3L) coverage. These distinct regions are easily identifiable in the paired THz-SNOM images. The red star and the black line in Fig. 1l indicate the start and path of a $30 \mu\text{m}$ line scan where we recorded the THz time-domain waveform for each position, as discussed below. Finally, Figures 1i,m show an example of a graphene flake with regions ranging from 1L to 6L, each with distinct contrast in the THz-SNOM image.

In addition to the contrast between various layer structures and local variations of the scattering signal within each layered region, we also observed localised dark spots in the THz-SNOM images, most likely due to polymer residuals and impurities from the transfer process and the subsequent short-term storage in an ambient atmosphere.

In addition to the white-light scans in Fig. 1, we performed a recording along the $30 \mu\text{m}$ path indicated in Fig. 1l. The step size was 200 nm , and a full THz time-domain trace was recorded at each position. The reference was formed by the average of the first 10 time traces on the substrate. These time-domain traces are summarised in Fig. 2a, where the color coding indicates the detected amplitude of the third-order demodulated signal $S_3(\tau)$, where τ is the THz time delay. The horizontal dashed lines indicate the boundaries between the layers observed in the white-light scan. The signal

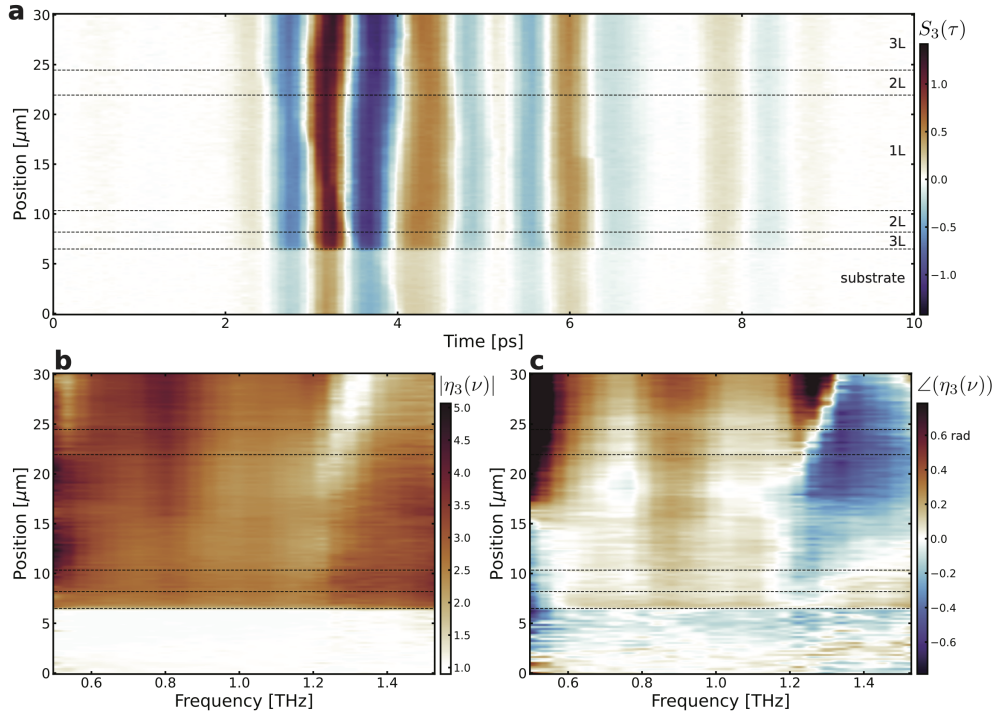


Fig. 2 Full THz-TDS line scan along the path shown in Fig. 1l. (a) Time-domain scattering signals $S_3(\tau)$ as a function of the THz time delay τ and position along the line scan path. (b) Frequency-resolved scattering ratio amplitude along the line scan. (c) Frequency-resolved scattering ratio phase along the line scan. Horizontal, dashed lines indicate the domain boundaries between the different layer regions.

increases significantly within the graphene area, but the boundaries between different layer counts are not visible. On the other hand, we observe a significant variation of the pulse shape along the line scan, visible as a slight drift and breathing of the vertical traces of the signal. Figure 2b shows the spectral variation of the ratio of the scattered signal magnitude on graphene relative to the substrate ($|\eta_3|$). Despite the expected relatively flat spectral response of the conductivity of graphene (see below), there is a significant structure in the spectrally resolved contrast. Figure 2c shows the associated variations in the spectral phase relative to that of the substrate.

The observation that the white-light scans (Fig. 1) show clear contrast variations as a function layer number and position, but that the contrast is not visible in the spectrally resolved line scan indicates that factors other than the local conductivity of graphene contribute to the detected signal. Due to the strong spectral variations of the signal we suspect that standing wave patterns on the AFM tip shaft and cantilever strongly interfere with the spectroscopic measurements. A simple estimate of the resonance frequency of a cantilever and tip of total length $280 \mu\text{m}$ in the experiment is given by $\nu = c/2L = 0.53 \text{ THz}$. The geometry of the tip and the cantilever is more complicated than this simple estimate can account for, and a full three-dimensional

simulation, including the support chip, the cantilever, and the shank would therefore be required to determine the influence of the tip shape on the scattered signal [39]. However, we observe an oscillation of the scattered signal with a spectral periodicity consistent with this estimated simple resonance criterion. Furthermore, we observe the modulation of the scattering ratio gradually increases as the tip is moved onto the graphene sample. This may be an indication that the effective far-field reflection coefficient r_p increases as the tip moves onto the more conductive region of the sample, and that the standing wave pattern then forms more efficiently. Taking all these factors into account in a quantitative manner is exceedingly difficult, and unfortunately hinders truly quantitative nanoscale spectroscopy in the THz range with current tip technology.

2.4 Theory and simulation of THz-SNOM response

Based on typical mobility values reported for exfoliated graphene under ambient conditions ($\mu \approx 5000 \text{ cm}^2/\text{Vs}$), we will use a Fermi energy of 0.1 eV and an electron scattering time of 50 fs in the following, unless otherwise noted.

In a THz-SNOM experiment, the strong localisation of the long-wavelength optical field under the tip leads to a large in-plane momentum of the THz field. Thus, the near-field interaction with a sample involves the exchange of this large momentum with the material. For a frequency of 1 THz, the free-space momentum of the electromagnetic field is $k_0 = \omega/c \approx 2.1 \times 10^4 \text{ m}^{-1}$, so the dominant in-plane wavenumber under a tip with $R = 50 \text{ nm}$ is $q \approx 1/R = 2 \times 10^7 \text{ m}^{-1}$, thus almost three orders of magnitude larger than k_0 . This enormous mismatch between q and k_0 in the THz range marks a prominent fundamental difference between s-SNOM in the infrared region and the lower part of the THz range ($< 2 \text{ THz}$). In the IR, the mismatch between the far-field and near-field in-plane momenta may instead be a factor of just 30 (the same estimate using a wavelength of 1550 nm), so in that sense THz-SNOM is much deeper in the near-field regime than a corresponding IR-SNOM measurement. Hence, it is possible to enter deep into the regime of non-local response of 2D materials with THz-SNOM [43].

Momentum conservation leads to a shift in the Drude absorption weight in graphene from DC to a finite frequency $\omega = v_F q$, where $v_F \approx 10^6 \text{ m/s}$ is the Fermi velocity [44]. This effect is illustrated schematically in Fig. 3a,b. For a dominant in-plane momentum $q \approx 2 \times 10^7 \text{ m}^{-1}$, the intraband transitions will peak at a frequency of approximately 3.2 THz. For a moderate electron scattering time $\tau = 50 \text{ fs}$, the mean free path of electrons in graphene is $L_{\text{mf}} = v_F \tau = 50 \text{ nm}$, comparable to the radius of the tip, and the locally enhanced electric field under the tip, therefore, varies on the length scale of L_{mf} . Local conductivity response models such as the Kubo formula [45] are based on a constant electric field. It is thus likely that the conductivity spectrum is influenced by non-local responses in the low-frequency range. Lovat *et al.* derived an analytical approximation of the non-local conductivity of graphene [46]. Figure 3c,d shows this analytical result calculated for the local and non-local conductivity of graphene at different Fermi energy levels (0-0.4 eV), showing the strong contrast between the local and non-local response in the low THz range. The relevant expressions are shown in the Supplementary Information.

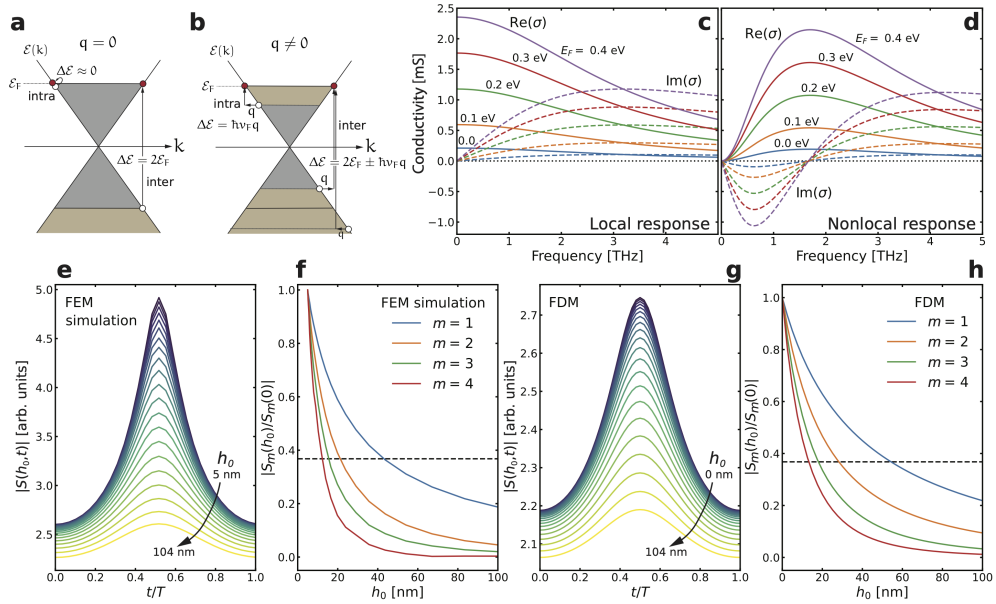


Fig. 3 Schematic illustration of interband and intraband (THz) transitions within the Dirac cone of the graphene band structure (adapted from Ref. 44) and conductivity spectrum of (a,c) local and (b,d) non-local graphene response, with conductivity plotted for a range of Fermi energies from 0 to 0.4 eV. The solid and dashed curves represent the real and imaginary parts of the conductivity, respectively. The non-local response is calculated at in-plane momentum $q = 14.2 \mu\text{m}^{-1}$. (e) Time-dependent scattering signal amplitude for logarithmically varying minimum tapping height and (f) normalised approach curves for the $m = 1, 2, 3, 4$ harmonics of the tapping frequency, obtained from FEM simulation. (g) and (h) are the same as (e) and (f), but calculated with the Finite Dipole Model (FDM).

Figure 3e,f shows an example of a FEM simulation run on a model system with monolayer graphene on a SiO_2/Si substrate where a THz-SNOM approach curve is simulated for a tapping amplitude of 100 nm. The minimum height h_0 is varied between 5-100 nm in a logarithmic manner, and for each height, the tapping sequence was simulated at a frequency of 1 THz. Figure 3e shows the time-domain results of the scattering signal $S(t)$ for the different initial heights (top curve: $h_0 = 5$ nm). The harmonic orders of the Fourier decomposition of each curve are shown in Fig. 3f for demodulation orders $m = 1 \dots 4$. The typical behaviour of the THz-SNOM approach curves is observed, with a biexponential decay and e^{-1} decay length in the 45-15 nm range. Figure 3g,h shows the corresponding results using the analytical FDM. The results are comparable to those obtained in the FEM simulation but with a lower height variation in the time domain. The calculated approach curves display decay lengths similar to those obtained by the FEM simulation.

Figure 4 summarises a comparison between FEM simulations and the analytical FDM model and demonstrates that the FEM shows a significantly larger signal contrast than the FDM model. In Fig. 4a, we show the scattering ratio $\eta_3(\nu)$ as a function of the THz frequency ν , which is the ratio of the demodulated scattering signal magnitudes $S_3(\nu)$ (demodulation order $m = 3$) with the s-SNOM tip over graphene

relative to the SiO₂/Si substrate. The curve shown in grey is the average value of the scattering ratio over the 0.2-2 THz range and shows a significant variation between values of 4 and 5.7 for Fermi energy levels 0.0-0.4 eV. For comparison, Fig. 4b,c shows the expected contrast calculated by the FDM with local and non-local conductivity response, respectively. Here the THz-SNOM contrast decreases slightly with increasing Fermi energy (local response) and increases steeply at the lowest Fermi energies, followed by a levelling off in the case of non-local response. In both cases, the contrast variation is low (-0.15 and +0.25 for a local and non-local response, respectively, in the 0.0-0.4 eV range of the Fermi energy).

Based on these fundamental results, we performed a spatially resolved FEM simulation on a monolayer graphene sheet (width 50 μm) across the frequency range 0.2-2.0 THz, as shown in Fig. 4d. The colour map shows the frequency-resolved contrast magnitude $|\eta_3(\nu)|$, and the curve shown in grey is the frequency-averaged scattering ratio. The average scattering ratio is approximately 5, and the effect of the edges is seen as small modulations of the scattering signal. Figure 4e shows the result of a similar FEM simulation where the model graphene sample now consists of zones with 1, 2 and 3 layers (1L, 2L, and 3L). The conductivity of multilayer graphene is assumed to scale linearly with the number of layers (see Supplementary Information). As expected from single-point simulations, the simulated scattering contrast increases with the layer count. The average scattering ratio (curve shown in grey) shows a layer contrast of 1.05 and 1.17, respectively, when moving from 1 layer to 2 and 3 layers. Hence, the experimentally measurable contrast is also present in the FEM simulations. We also observe that the contrast depends on the position of the sample. In Fig. 4, the tip is illuminated by a plane-wave from the direction of negative positions to positive positions, and we find that the layer contrast is clearest in the sample's top half (positive positions). This observation is likely due to interference with edge-launched plasmonic surface modes in graphene [47].

The simulated sample structure in Fig. 4 is similar to the line scan across one of the graphene samples, as shown in Fig. 11. Hence, we can directly compare the experimentally observed contrast with the FEM results. This comparison is shown in Fig. 5. Here the experimental contrast along the line scan is shown, and we show the average scattering ratio relative to that obtained in the region of monolayer graphene (position 15-22 μm). The first four demodulation orders ($m = 1 \dots 4$) are shown. For $m = 3$, the experimental contrast with monolayer graphene is 1.04 (two layers) and 1.14 (three layers), comparable to the contrast observed in FEM simulations. It is tempting to directly compare the specific contrast values between the experiment and the FEM simulation. However, several factors hinder such a comparison. First, the assumption in the FEM simulation that the conductivity scales linearly with the layer count is oversimplified. Second, the absolute value of the contrast in the FEM simulation depends on a typical Fermi energy level of the graphene that has not been confirmed for our specific samples. However, the contrast comparison allows us to conclude that the experimental THz-SNOM contrast can be explained by the same effects included in the FEM simulation, namely the electromagnetic interaction in the local regime.

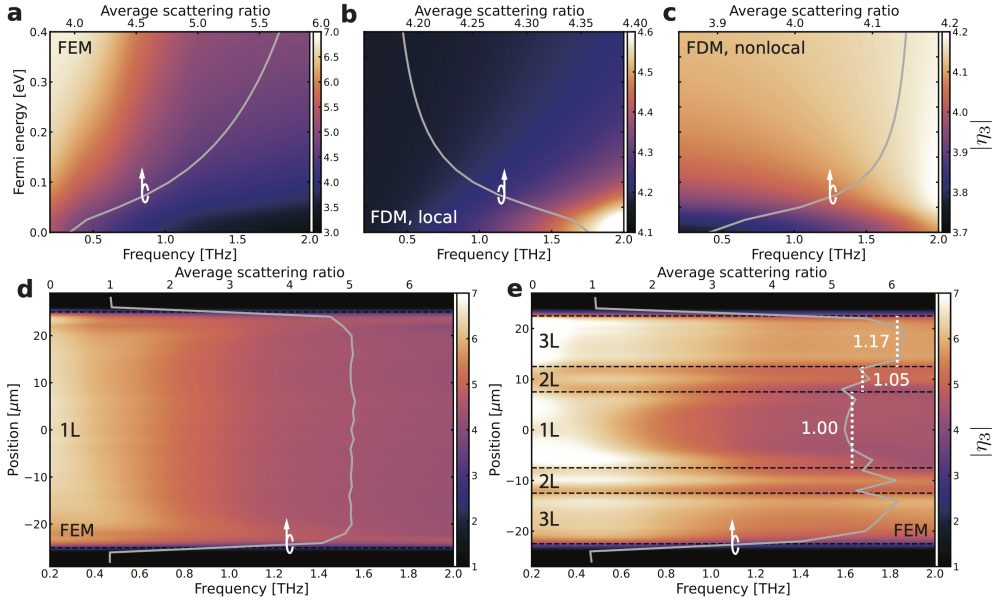


Fig. 4 (a,b,c) Scattering ratio $|\eta_3|$ from graphene relative to that of a SiO_2/Si substrate, as a function of the incident THz frequency and the Fermi energy of graphene. (a) Finite-element (FEM) simulation, (b) Finite Dipole Model (FDM) with local response, and (c) FDM with non-local response of graphene, using $q = 14.2 \mu\text{m}^{-1}$. (d,e) Spectrally and spatially resolved FEM simulation of the amplitude of the scattering ratio $|\eta_3|$ of a $50 \mu\text{m}$ wide graphene strip on a SiO_2/Si substrate. The simulated graphene samples consist of (d) a monolayer and (e) a structure with 3-2-1-2-3 layers from top to bottom, where the black dashed lines and values indicate the contrast of 2 and 3 layers relative to monolayer graphene. Top axis in all panels: The grey curves show the frequency-averaged scattering signal. All results are evaluated for the harmonic order of $m = 3$.

3 Methods

Sample Preparation

Graphene samples were prepared by mechanical exfoliation of graphite (NGS Naturgraphit GmbH) on silicon wafers with a 90 nm thick thermal SiO_2 layer, resulting in a wide range of graphene flakes with various thicknesses distributed on the same substrate. Optical microscopy was then used to identify suitable monolayer and few-layer flakes on the surface, and to assess the number of graphene layers on a given sample based on the optical contrast [48, 49].

Experimental details and data extraction

THz-SNOM is performed with a commercial s-SNOM system (Attocube THz-NeaSCOPE) equipped with an integrated THz time-domain spectroscopy module (Attocube/Menlo Systems TeraSmart). THz pulses are generated and detected by photoconductive antennas, and the integrated system has a useful signal-to-noise ratio in the frequency band 0.5–2 THz. The system operates as an atomic force microscope

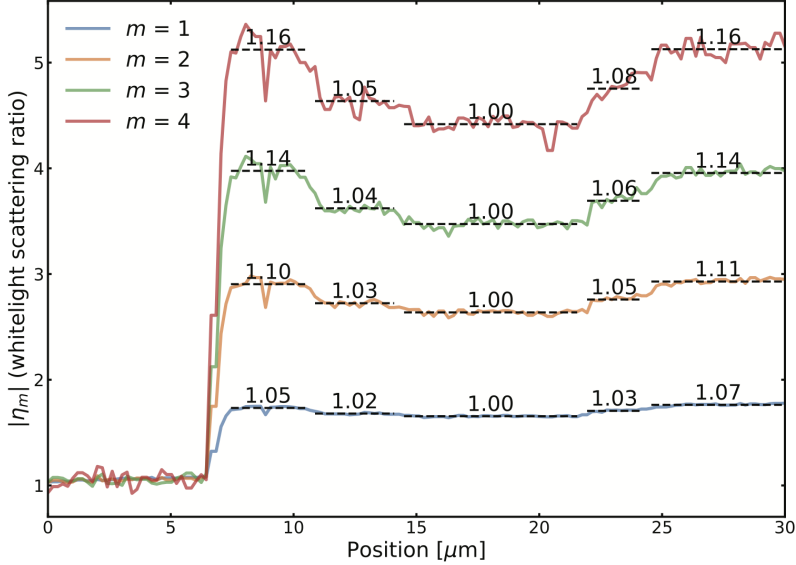


Fig. 5 Experimentally measured THz-SNOM contrast along the scan line indicated in Fig. 11, for demodulation orders $m = 1 - 4$.

(AFM), with optical access to the AFM tip. The THz beam is guided and focused via reflective optics onto the AFM tip, and identical optics guide the scattered THz light from the AFM tip to the detector. We used solid PtIr AFM tips with a tip shank length of $80 \mu\text{m}$ (Rocky Mountain Nanotechnology, 25PtIr200B-H). We operated the THz-SNOM system in an atmosphere purged with nitrogen (N_2) gas to minimise water vapour absorption lines in the detected THz spectra. A schematic of the AFM tip on a sample with the incident and scattered THz radiation is shown in Fig. 1a.

The THz-SNOM signal is recorded with the AFM operating in tapping mode, as is standard in most modern SNOM systems. Briefly, the time-dependent scattered signal $S(t)$ is detected in real-time and demodulated at the overtones S_m of the tapping frequency Ω to suppress the far-field background signal. Here m is the demodulation order, typically $m = 2 - 4$. Therefore, a time trace of a scattered THz signal is represented as $S_m(\tau)$, where τ is the time delay along the THz time axis, as shown in Fig. 1b. The frequency spectra of these two signals are shown in Fig. 1c, covering the 0.5–1.6 THz range.

FEM Simulations

In the finite-element modelling (FEM) of the tip-sample interaction we represent the scattered THz signal as the integrated y -component of the electric field on the surface of the AFM tip, as indicated in Fig. 1a. We used the commercial software COMSOL Multiphysics to simulate the electromagnetic scattering of THz fields from the AFM tip in the THz-SNOM experiment. Following the methods described by Conrad *et al.* [37], we simplified the simulation domain to 2D, allowing a sufficiently fine meshing

for accurate representation of the scattered field, and to support extended parameter sweeps of spectrally and spatially resolved simulations.

Graphene was modelled as an infinitely thin transition layer with intraband sheet conductivity $\sigma_{\text{intra}}(\omega)$ described by the Kubo formalism, as detailed in the Supplementary Information. Multilayer graphene was, for simplicity, modelled as $\sigma_N(\omega) = N\sigma_{\text{intra}}(\omega)$. Although simple, this representation is in reasonable agreement with the overall trend observed in DC conductivity measurements on multilayer samples [50]. We included a layer of SiO₂ (thickness 90 nm, $\epsilon_{\text{SiO}_2} = 3.88$) on top of the Si substrate ($\epsilon_{\text{Si}} = 11.68$). For the main simulations, the tip was modelled as an ellipsoid with a major semi-axis length of $L_a = 40 \mu\text{m}$ (total tip length $L = 2L_a$), radius of curvature of $R = 50 \text{ nm}$, and the resulting minor semi-axis length $L_b = \sqrt{R \times L_a} \approx 1.4 \mu\text{m}$. Supplementary information shows additional simulation results with variations of L and R .

The simulation domain was surrounded by scattering boundary conditions, and excited in the frequency domain by a plane wave incident from the top left at an angle of 30 degrees from vertical. We used incident frequencies between 0.2 and 2 THz in the simulations.

On average, the meshing process resulted in approximately 2.1×10^6 cells adaptively distributed over the simulation area of $500 \times 500 \mu\text{m}^2$. Further details are given in the Supplementary Information.

4 Conclusion

We have shown that despite theoretical models predicting a lack of contrast in highly conducting samples and notable supporting experiments, THz-SNOM can in fact detect small variations in the local conductivity of graphene samples, not only enabling the differentiation of the number of graphene layers in a multilayer sample but even enabling detailed inspection of the local variations of the conductivity within monolayer graphene samples. The observed contrast cannot be explained by the finite dipole model, although the inclusion of the nonlocal response of graphene enabled the FDM to predict the experimentally observed trend of higher contrast with higher conductivity of graphene. On the other hand, the observed contrast could almost be quantitatively reproduced by a simple finite-element simulation without nonlocal effects. This shows that the unexpected contrast is rooted in a classical electromagnetic interaction and suggests that the FDM can be expanded to consider thin layers of high, finite conductivity.

Our work strongly suggests that spectrally resolved THz-SNOM can—contrary to expectations—be a powerful tool for quantitative measurements of the conductivity spectrum and, therefore, for determining both the DC conductivity and the scattering rate of conductive 2D materials and thin ($< 10 \text{ nm}$) films of metals. Uniquely, this information can be extracted at a scale that is smaller or comparable with the transport lengths, such as the mean free path or coherence length. THz-SNOM will be invaluable for unravelling local transport properties in quantum materials and systems, including correlated conductors, topological materials, twistronics, straintronics, and spintronics, just as it could be highly suitable for optimisation and process

development of 2D materials within a commercial context. Future improvements in tip design that suppress standing waves on the cantilever and shank would further enable the application of spectroscopic THz-SNOM to investigate conductive surfaces at the nanoscale.

Supplementary information. Supplementary information available.

Acknowledgements. We thank Martijn Wubs, Nicolas Stenger and N. Asger Mortensen for valuable discussions on non-local response in electrodynamics. We acknowledge partial financial support from the Danish Independent Research Fund (projects ULTRA-TED, ULTRA-LOWD, and Tr2DEO), the NNF Challenge Program BIOMAG, the Villum Foundation (IonGate), and the Carlsberg Foundation (DEEP-MAP).

S1 Supplementary information

Supplementary information on local and nonlocal conductivity models, experimental THz-SNOM results on graphene, reproducibility of results, and simulation details.

S1.1 Local and nonlocal conductivity of graphene

Using the Kubo formalism, the intraband conductivity of graphene in the local limit can be written as [51]

$$\sigma_{\text{intra}}(\omega) = \frac{2k_B T e^2 \tau}{\pi \hbar^2} \ln \left(2 \cosh \frac{E_F}{2k_B T} \right) \frac{1}{1 - i\omega\tau}, \quad (\text{S1})$$

where E_F is the Fermi energy, τ is the electron scattering time, T is the temperature, and k_B is the Boltzmann constant.

In a THz-SNOM experiment the strong localization of the long-wavelength optical field under the tip leads to a large in-plane momentum of the THz field. Thus, the near-field interaction with a sample involves exchange of this large momentum with the material.

The relevant value of q is determined by the localization of the electric field under the tip, which in turn is determined by the radius of curvature R of the tip so that $q \approx 1/R$, which for a 50-nm radius of curvature gives $q \approx 2 \times 10^7 \text{ m}^{-1}$. Within the framework of the point dipole model (see below), the dominant in-plane momentum can be calculated as the maximum of the weight function $q^2 \exp(-2q(R + \frac{1}{2}A(1 - \cos(\Omega t))))$ averaged over a tapping cycle [52],

$$W(A, R, q) = 2\pi q^2 e^{-2q(R+A)} I_0(2qA), \quad (\text{S2})$$

where $I_0(x)$ is the modified Bessel function of the first kind of real order. For a tapping amplitude $A = 100 \text{ nm}$ and a tip radius $R = 50 \text{ nm}$ the weight function peaks at $q \approx 1.4 \times 10^7 \text{ m}^{-1}$, in reasonable agreement with the simpler estimate $q \approx 1/R$.

Lovat et al. [46] developed a semiclassical model for the nonlocal intraband transverse and longitudinal conductivity of graphene with a convenient closed-form formulation, derived from the semiclassical Boltzmann transport equation under the Bhatnagar-Gross-Krook (bgk) model [53] that, as the Mermin correction [54] to the Lindhard model, assures local charge conservation.

$$\sigma_T^{(bgk)}(q, \omega) = \gamma \frac{2\pi\alpha}{v_F^2 q^2} (1 - \chi), \quad (\text{S3})$$

$$\sigma_L^{(bgk)}(q, \omega) = \frac{v_F}{2\pi\gamma_D(1 - \chi) + v_F\chi} \sigma_T^{(bgk)}, \quad (\text{S4})$$

$$\chi = \sqrt{1 - \frac{v_F^2 q^2}{\alpha^2}}, \quad (\text{S5})$$

$$\gamma = i \frac{e^2 k_B T}{\pi^2 \hbar^2} \ln \left[2 \left(1 + \cosh \left(\frac{E_F}{k_B T} \right) \right) \right], \quad (\text{S6})$$

Parameter	Value
L	600 nm
R	50 nm
W_0	$1.31R$
W_1	$R/2$
g	0.7
q	$1.42 \times 10^7 \text{ m}^{-1}$
$H(t)$	$\frac{1}{2}A(1 + \cos \Omega t)$
A	100 nm
Ω	83 kHz

Table 1 Parameters used in FDM calculations

$$\gamma_D = -i \frac{v_F}{2\pi\omega\tau}, \quad (\text{S7})$$

$$\alpha = \omega + i/\tau. \quad (\text{S8})$$

In the local limit ($q \rightarrow 0$) the Lovat model reduces to the Kubo formula, Eq. (S1).

S1.2 THz-SNOM: Finite dipole model

The finite dipole model (FDM) [27, 55] is an electrostatic model that describes the polarizability of a spheroidal, metallic tip close to a surface. The FDM takes a finite size of the tip into account and thus extends the point dipole model (PDM) [9, 26]. In both the FDM and the PDM, the scattered electric field from the dipole representing the tip-surface system is

$$E_{\text{sca}} = (1 + r_p)^2 \alpha_{\text{eff}} E_{\text{inc}}, \quad (\text{S9})$$

where E_{inc} is the incident electric field, α_{eff} is the effective polarizability of the tip-sample system. The prefactor $(1 + r_p)^2$ is the far-field Fresnel reflection factor taking specular reflection of the incident and scattered fields into account. The tip extends in the vertical (y) direction, scattering the y component of the electric field, corresponding to p polarization.

Following the notation used by Hauer et al. [56], the effective polarizability is in the FDM defined by the near-field (quasi-electrostatic) reflection coefficient β and two geometric function f_0 and f_1 ,

$$\alpha_{\text{eff}} \propto 1 + \frac{1}{2} \frac{\beta f_0}{1 - \beta f_1}, \quad (\text{S10})$$

$$f_{0,1} = \left(g - \frac{R + 2H + W_{0,1}}{2L} \right) \frac{\ln \frac{4L}{R + 4H + 2W_{0,1}}}{\ln \frac{4L}{R}}. \quad (\text{S11})$$

Here $g \approx 0.7$ is an empirical factor [27, 55], R is the radius of curvature of the tip, H is the height from the sample surface to the tip, $W_0 \approx 1.31R$ and $W_1 \approx R/2$ are the approximate positions of the point charge representing a fictual point monopole Q_0 and a near-field induced monopole Q_1 , and L is the half of the length of the spheroidal dipole. Table 1 summarizes the parameters used in our FDM calculations.

The scattered field contains both far-field and near-field information. The far-field contribution can be effectively suppressed by tapping of the tip at some frequency Ω and detection of the scattered signal at a higher harmonic $\Omega_m = m\Omega$. The height over the surface of the tip is modulated as $H(t) = h_0 + \frac{1}{2}A(1 + \cos(\Omega t))$, and the harmonic orders of the scattered signal is recovered by Fourier decomposition of the time-dependent signal,

$$E_{\text{sca}}(\Omega_m) = \int_0^T E_{\text{sca}}(t) e^{i\Omega_m t} dt = (1 + r_p)^2 \alpha_{\text{eff,m}} E_{\text{inc}} \quad (\text{S12})$$

where T is the tapping period.

The near-field reflection coefficient β is, for an infinite, homogeneous substrate with relative permittivity ϵ , given by $\beta = (\epsilon - 1)/(\epsilon + 1)$. This relation is the electrostatic version of the Fresnel reflection coefficient for p -polarized electric fields and is derived in the limit of infinite in-plane momentum q of the electric field. In the quasi-electrostatic case where the frequency of the electromagnetic field is low but nonzero, and the substrate under the tip is covered by an infinitely thin conductive film with (possibly nonlocal) sheet conductance $\sigma_s(\omega, q)$ the expression is replaced by a more general $\beta(\omega, q)$ [52],

$$\beta(\omega, q) = \frac{\epsilon_2 - \epsilon_1 \sqrt{\frac{\epsilon_2 \omega^2 / c^2 - q^2}{\epsilon_1 \omega^2 / c^2 - q^2}} + \frac{\sigma_s}{\epsilon_0 \omega} \sqrt{\epsilon_2 \omega^2 / c^2 - q^2}}{\epsilon_2 + \epsilon_1 \sqrt{\frac{\epsilon_2 \omega^2 / c^2 - q^2}{\epsilon_1 \omega^2 / c^2 - q^2}} + \frac{\sigma_s}{\epsilon_0 \omega} \sqrt{\epsilon_2 \omega^2 / c^2 - q^2}}. \quad (\text{S13})$$

In the experiments presented in this paper, the graphene samples are deposited on an SiO_2/Si substrate, with 90 nm thickness of the SiO_2 layer. We, therefore, need to incorporate the thin oxide layer in the modeling of the near-field reflection coefficient. We follow the matrix-based method first described by Zhan *et al.* [57] and later by Wirth *et al.* [34] where the reflection from a layered sample is modeled by 2×2 matrices representing each interface and layer in the stack.

The matrices $\underline{\mathbf{D}}_{12}$ and $\underline{\mathbf{D}}_{23}$ are the transfer matrices for p -polarized light across the interface between air and SiO_2 and the SiO_2/Si interface, respectively,

$$\underline{\mathbf{D}}_{12} = \frac{1}{2} \begin{bmatrix} 1 + \eta_{12} + \xi_{12} & 1 - \eta_{12} - \xi_{12} \\ 1 - \eta_{12} + \xi_{12} & 1 + \eta_{12} - \xi_{12} \end{bmatrix}, \quad \underline{\mathbf{D}}_{23} = \frac{1}{2} \begin{bmatrix} 1 + \eta_{23} & 1 - \eta_{23} \\ 1 - \eta_{23} & 1 + \eta_{23} \end{bmatrix},$$

$$\eta_{12} = \frac{\epsilon_1 k_{2z}}{\epsilon_2 k_{1z}}, \quad \xi_{12} = \frac{\sigma_s k_{2z}}{\epsilon_0 \epsilon_2 \omega}, \quad \eta_{23} = \frac{\epsilon_2 k_{3z}}{\epsilon_3 k_{2z}}. \quad (\text{S14})$$

Here $k_{iz} = \sqrt{\epsilon_i k_0^2 - q^2}$ is the out-of-plane wave number in medium i and ϵ_i is the permittivity of medium i ($i = 1$: air, $i = 2$: SiO_2 , $i = 3$: Si).

The propagation matrix through the SiO₂ spacer layer of thickness d_{SiO_2} is

$$\underline{\mathbf{P}}(\Delta z) = \begin{bmatrix} e^{-ik_z \Delta z} & 0 \\ 0 & e^{ik_z \Delta z} \end{bmatrix}. \quad (\text{S15})$$

The full transfer matrix of the layered structure is then $\underline{\mathbf{M}} = \underline{\mathbf{D}}_{12} \underline{\mathbf{P}} \underline{\mathbf{D}}_{23}$. For a conductive film directly on a semi-infinite substrate, $\underline{\mathbf{M}} = \underline{\mathbf{D}}_{12}$. In both cases the near-field reflection coefficient $\beta(\omega, q)$ is then extracted from the elements of $\underline{\mathbf{M}}$,

$$\beta(\omega, q) = \frac{M_{21}}{M_{11}}. \quad (\text{S16})$$

Figure S6 plots $\beta(\omega, q)$ for two geometries. The two top rows are calculated for graphene deposited directly on a silicon substrate (two media, $\epsilon_1 = 1, \epsilon_2 = 11.7$), and the bottom two rows are calculated for graphene on a SiO₂/Si structure (three media, $\epsilon_1 = 1, \epsilon_2 = 3.8, \epsilon_3 = 11.7, d_{\text{SiO}_2} = 90$ nm). Rows 1,3 show the amplitude, and rows 2,4 show the phase of $\beta(\omega, q)$. The left column shows $\beta(\omega, q)$ for the substrate without graphene film, the center column shows $\beta(\omega, q)$ using the local conductivity of graphene, and the right column is calculated using the nonlocal response of graphene. Graphene is represented by a Fermi energy of 0.1 eV, a scattering time of 50 fs, and a temperature of 300 K. The vertical dashed line in all plots shows the dominant in-plane momentum for a tip radius of curvature of 50 nm and a tapping amplitude of 100 nm (see Eq. (S2)). The dashed curves show the light line ($\omega = qc$).

S1.3 FEM simulations

We use the commercial software COMSOL Multiphysics to simulate the electromagnetic scattering of THz fields from the AFM tip in the THz-SNOM experiment. Following the methods described by Conrad *et al.* [37], we simplify the simulation to 2D. This enables sufficiently fine meshing and the extended parameter sweeps required for broadband, spatially resolved simulations of the experiments.

Graphene was modeled as an infinitely thin transition layer with sheet intraband sheet conductivity given by Eq. (S1). Multilayer graphene was, for simplicity and the lack of a more precise representation, modeled as $\sigma_N(\omega) = N\sigma_{\text{intra}}(\omega)$. While this representation is a stark simplification, it agrees reasonably with the overall trend observed with DC conductivity measurements on multilayer samples [50]. We included a SiO₂ layer (thickness 90 nm, $\epsilon_{\text{SiO}_2} = 3.88$) on top of the Si substrate ($\epsilon_{\text{Si}} = 11.68$). The tip was modeled as a spheroidal shape with a major semiaxis length of $L_a = 40$ μm , a radius of curvature of $R = 50$ nm, and resulting minor semiaxis length $L_b = \sqrt{R \times L_a} \approx 1.4$ μm . The tip material was modeled as a Drude metal with the finite conductivity of a typical good conductor.

The simulation domain was surrounded by scattering boundary conditions and excited in the frequency domain by a plane wave incident from the top left at an angle of 30 degrees from vertical. We used incident frequencies between 0.2 and 2 THz in the simulations.

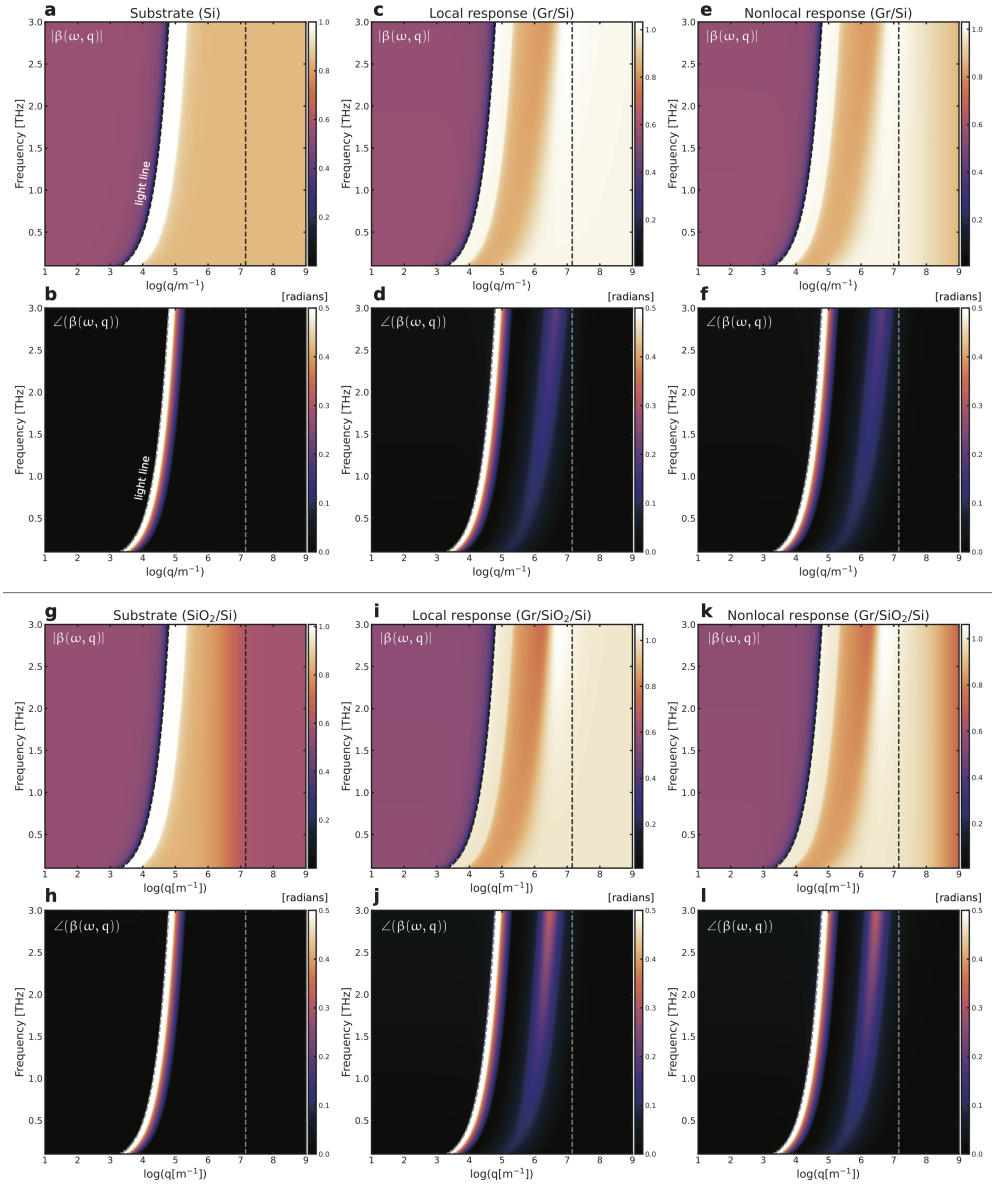


Fig. S6 Near-field reflection coefficient $\beta(\omega, q)$. The amplitude is shown in (a,c,e,g,i,k), and the phase is shown in (b,d,f,h,j,l). (a-f) Semi-infinite silicon substrate. (a,b) Silicon substrate alone, (c,d) graphene on silicon with a local response of graphene, (e,f) graphene on silicon with a nonlocal conductivity response of graphene. (g-l) shows the same calculations with graphene on a SiO_2/Si substrate.

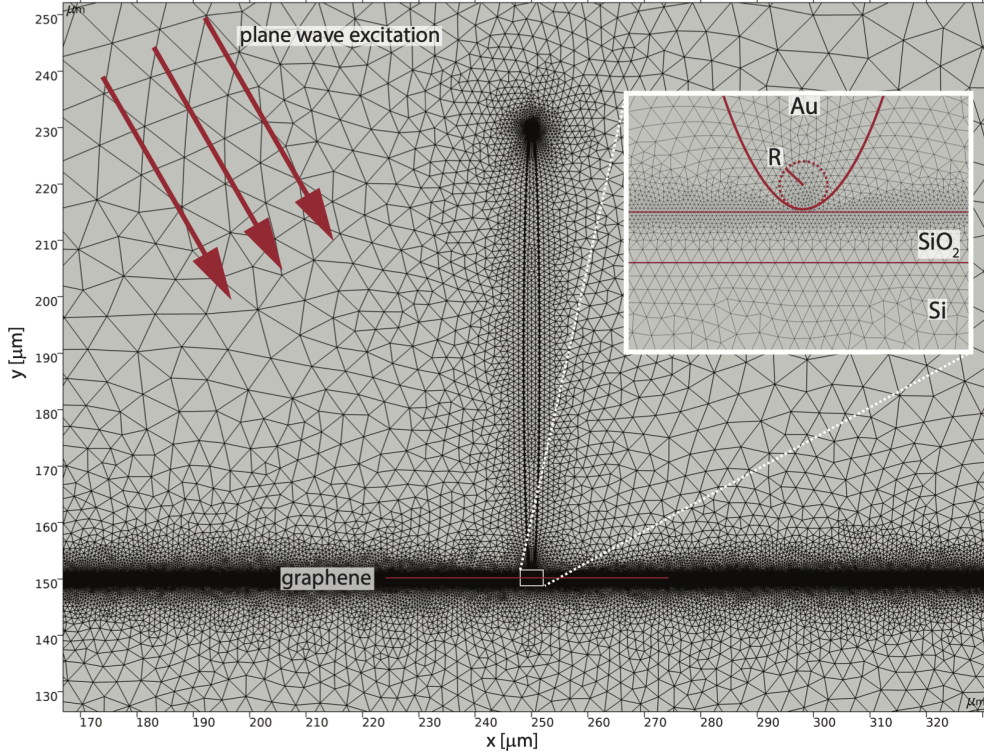


Fig. S7 Meshing of the 2D model of the tip-sample system in COMSOL. Inset shows the apex of the tip close to the graphene sheet on the SiO_2/Si substrate.

The meshing on average included approximately 2.1×10^6 cells adaptively meshed over the simulation area of $500 \times 500 \mu\text{m}^2$, as illustrated in Fig. S7. The inset shows the meshing near the tip apex for the smallest tip-surface distance of 5 nm used in the simulation runs.

A simulation run consisted of individual simulations for 16 different tip heights over the sample according to the formula $h(t) = h_0 + \frac{1}{2}A(1 + \cos(2\pi t/T))$. We simulated half of the oscillation cycle of the tip. We used a tapping amplitude $A = 100$ nm and a minimum height $h_0 = 5$ nm. After each simulation, the scattered signal $S(h(t)) = S(t)$ was calculated as the y component of the electric field integrated over the full surface of the spheroidal tip shape. The Fourier components of the sequence $S(t)$ were then calculated and used as the final output of the simulation. Based on this scheme, sweeps over frequencies (0.2–2 THz), the Fermi energy of graphene (0–0.4 eV), and the lateral position of the graphene sheet on the surface could be performed.

A single calculation (one height h , one frequency ω) requires 10–15 s of simulation time, leading to a run time of approximately 200 s for the simulation of a full tapping cycle on a desktop computer (Intel i9-11900K, eight physical cores, 128GB memory).

In the main article, the calculated THz-SNOM contrast between graphene with a given conductivity and the substrate is shown for a tip length $L = 80 \mu\text{m}$ in Fig. 1b.

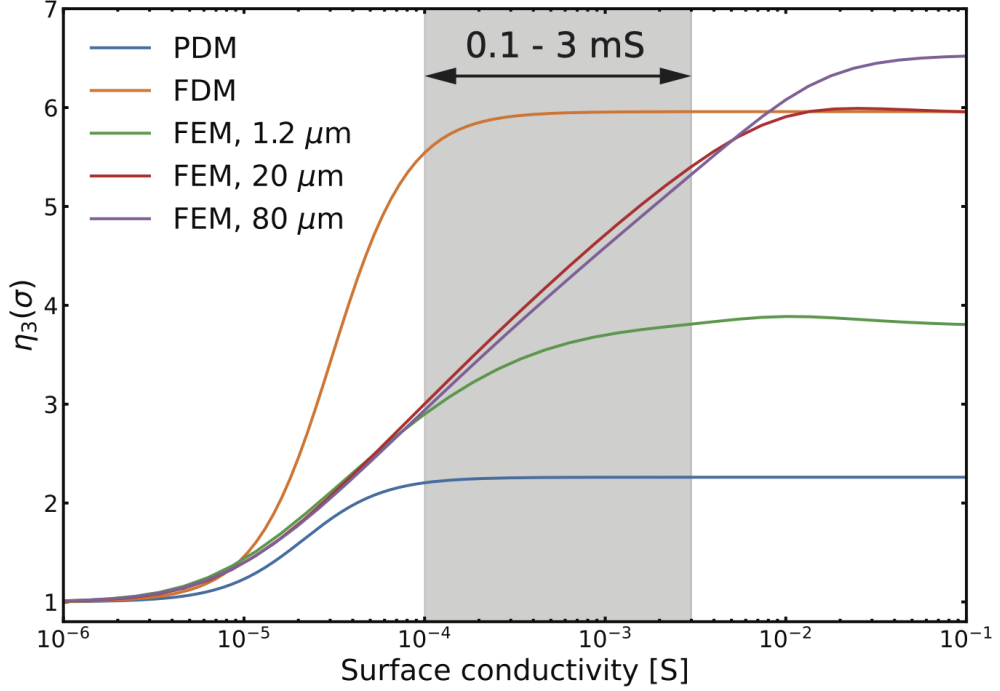


Fig. S8 Contrast between the scattered signal from graphene and from the substrate (90 nm SiO₂/Si) as predicted by the PDM, the FDM (tip length 1.2 μm , tip radius 50 nm), and FEM, with tip lengths as indicated.

For this calculation, we have used a frequency $\omega/2\pi = 1$ THz and a freely varying conductivity as indicated in the figure ($10^{-6} - 1$ S) instead of the Drude-like conductivity model. In Fig. S8, we further detail the influence of the tip length on the graphene-substrate contrast in the FEM simulation. The figure shows the contrast as a function of the conductivity of the graphene, in the range $10^{-6} - 1$ S, for tip lengths L of 1.2 μm , 20 μm , and 80 μm (major semi-axis lengths L_a of 600 nm, 20 μm , 40 μm). The gray area of the plot indicates the typical conductivity range of conductivities of exfoliated and CVD-grown graphene under ambient conditions.

The longer tips ($L = 20$ μm and 80 μm) display similar contrasts between the graphene and the substrate, and the short tip ($L = 1.2$ μm) shows a weaker contrast variation with conductivity. Hence, the FEM simulations indicate that for realistic tip lengths used in practice, the contrast variation with conductivity is only weakly dependent on the dimensions of the tip. We note that in the case of the FEM simulations, the absolute value of the contrast is not directly comparable with the contrast observed in experiments. The simulations are simplified to 2D, and the real shape of the full tip and cantilever is not considered.

Figure S9 shows the results of simulations with varying tip length and tip radius. The graphene conductivity is 1 mS, and the frequency is 1 THz in the simulations. Figure S9a,b shows the scattering ratio (graphene/substrate) when the tip length L

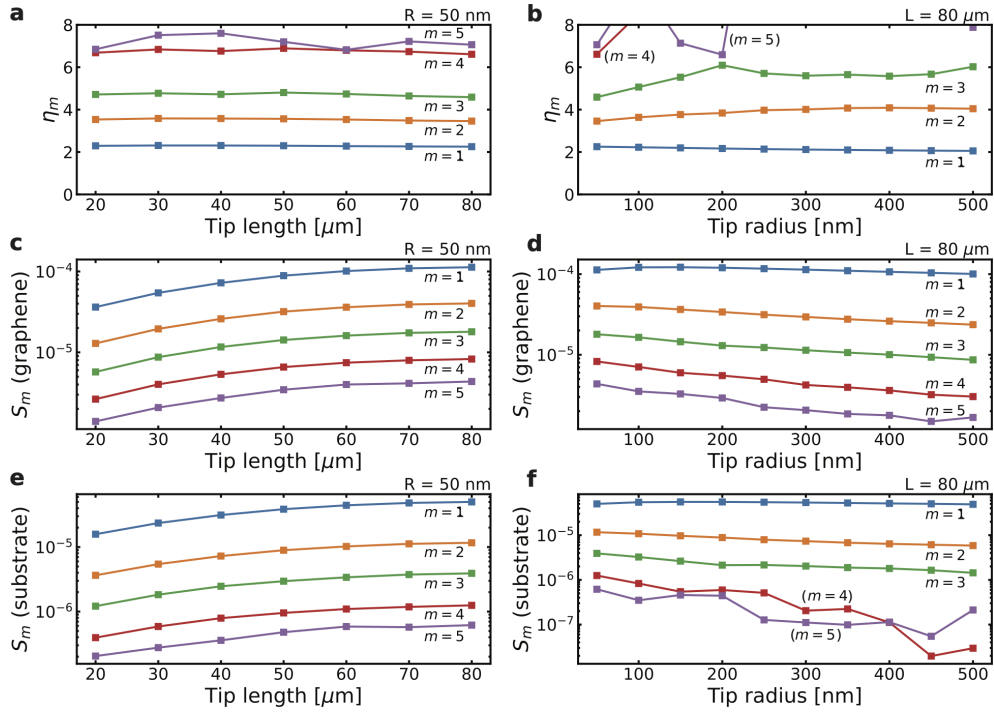


Fig. S9 Results of FEM simulations with varying tip length and tip radius. (a,b) The scattering ratio (graphene/substrate) with varying tip length L (a) and varying tip radius R (b). (c,e) and (d,f) Scattering signals from graphene and substrate for the parameter sweeps performed in (a,b). Data are shown for demodulation orders $m = 1 - 5$, with numerical noise influencing $m = 4, 5$ in (b) and (f).

is varied (Fig. S9a) and when the tip radius R is varied (Fig. S9b). Data are shown for demodulation orders $m = 1 \dots 5$, with numerical noise influencing $m = 4, 5$ in Fig. S9b. It can be seen that the scattering ratio is rather constant in the parameter space investigated here. Figure S9c,e and S9d,f shows the scattering signals from graphene and substrate for the parameter sweeps, used to form the scattering ratios in Fig. S9a,b. Here the simulation predicts that a longer tip results in a larger absolute scattering signal, as could be expected. On the other hand, the absolute signal strength is reduced slightly for larger radii of the tip.

References

- [1] Tomaino, J.L., Jameson, A.D., Kevek, J.W., Paul, M.J., Zande, A.M., Barton, R.A., McEuen, P.L., Minot, E.D., Lee, Y.S.: Terahertz imaging and spectroscopy of large-area single-layer graphene. *Optics Express* **19**(1), 141–146 (2011) <https://doi.org/10.1364/oe.19.000141>
- [2] Buron, J.D., Petersen, D.H., Bøggild, P., Cooke, D.G., Hilke, M., Sun, J., Whiteway, E., Nielsen, P.F., Hansen, O., Yurgens, A., Jepsen, P.U.: Graphene conductance uniformity mapping. *Nano Letters* **12**(10), 5074–5081 (2012) <https://doi.org/10.1021/nl301551a>
- [3] Bøggild, P., Mackenzie, D.M.A., Whelan, P.R., Petersen, D.H., Buron, J.D., Zurutuza, A., Gallop, J., Hao, L., Jepsen, P.U.: Mapping the electrical properties of large-area graphene. *2D Materials* **4**(4), 042003 (2017) <https://doi.org/10.1088/2053-1583/aa8683>
- [4] Whelan, P.R., Zhou, B., Bezencenet, O., Shivayogimath, A., Mishra, N., Shen, Q., Jessen, B.S., Pasternak, I., Mackenzie, D.M.A., Ji, J., Cunzhi, S., Seneor, P., Dlubak, B., Luo, B., Østerberg, F., Huang, D., Shi, H., Luo, D., Wang, M., Ruoff, R.S., Conran, B., McAleese, C., Huyghebaert, C., Brems, S., Booth, T., Napal, I., Strupinskii, W., Petersen, D.H., Forti, S., Coletti, C., Jouvray, A., Teo, K.B.K., Centeno, A., Zurutuza, A., Legagneux, P., Jepsen, P.U., Bøggild, P.: Case studies of electrical characterisation of graphene by terahertz time-domain spectroscopy. *2D Materials* **8**, 022003 (2021) <https://doi.org/10.1088/2053-1583/abdbcb>
- [5] Pohl, D.W., Denk, W., Lanz, M.: Optical stethoscopy: Image recording with resolution $\lambda/20$. *Applied Physics Letters* **44**(7), 651–653 (1984) <https://doi.org/10.1063/1.94865>
- [6] Zenhausern, F., O’Boyle, M.P., Wickramasinghe, H.K.: Apertureless near-field optical microscope. *Applied Physics Letters* **65**(13), 1623–1625 (1994) <https://doi.org/10.1063/1.112931>
- [7] Keilmann, F., Weide, D.W., Eickelkamp, T., Merz, R., Stöckle, D.: Extreme sub-wavelength resolution with a scanning radio-frequency transmission microscope. *Optics Communications* **129**(1–2), 15–18 (1996) [https://doi.org/10.1016/0030-4018\(96\)00108-3](https://doi.org/10.1016/0030-4018(96)00108-3)
- [8] Knoll, B., Keilmann, F., Kramer, A., Guckenberger, R.: Contrast of microwave near-field microscopy. *Applied Physics Letters* **70**(20), 2667–2669 (1997) <https://doi.org/10.1063/1.119255>
- [9] Knoll, B., Keilmann, F.: Enhanced dielectric contrast in scattering-type scanning near-field optical microscopy. *Optics Communications* **182**(4), 321–328 (2000) [https://doi.org/10.1016/S0030-4018\(00\)00826-9](https://doi.org/10.1016/S0030-4018(00)00826-9)

- [10] Liewald, C., Mastel, S., Hesler, J., Huber, A.J., Hillenbrand, R., Keilmann, F.: All-electronic terahertz nanoscopy. *Optica* **5**(2), 159–163 (2018) <https://doi.org/10.1364/OPTICA.5.000159>
- [11] Chen, X., Liu, X., Guo, X., Chen, S., Hu, H., Nikulina, E., Ye, X., Yao, Z., Bechtel, H.A., Martin, M.C., Carr, G.L., Dai, Q., Zhuang, S., Hu, Q., Zhu, Y., Hillenbrand, R., Liu, M., You, G.: Thz near-field imaging of extreme subwavelength metal structures. *ACS Photonics* **7**(3), 687–694 (2020) <https://doi.org/10.1021/acsp Photonics.9b01534>
- [12] Wiecha, M.M., Kapoor, R., Roskos, H.G.: Terahertz scattering-type near-field microscopy quantitatively determines the conductivity and charge carrier density of optically doped and impurity-doped silicon. *APL Photonics* **6**(12), 126108 (2021) <https://doi.org/10.1063/5.0070608>
- [13] Schäffer, S., Ogolla, C.O., Loth, Y., Haeger, T., Kreusel, C., Runkel, M., Riedl, T., Butz, B., Wigger, A.K., Bolívar, P.H.: Imaging the terahertz nanoscale conductivity of polycrystalline CsPbBr₃ perovskite thin films. *Nano Letters* (2023) <https://doi.org/10.1021/acs.nanolett.2c03214>
- [14] Chen, X., Liu, X., Guo, X., Chen, S., Hu, H., Nikulina, E., Ye, X., Yao, Z., Bechtel, H.A., Martin, M.C., Carr, G.L., Dai, Q., Zhuang, S., Hu, Q., Zhu, Y., Hillenbrand, R., Liu, M., You, G.: THz near-field imaging of extreme subwavelength metal structures. *ACS Photonics* **7**(3), 687–694 (2020) <https://doi.org/10.1021/acsp Photonics.9b01534>
- [15] Chen, S., Bylinkin, A., Wang, Z., Schnell, M., Chandan, G., Li, P., Nikitin, A.Y., Law, S., Hillenbrand, R.: Real-space nanoimaging of THz polaritons in the topological insulator Bi₂Se₃. *Nature Communications* **13**(1), 1374 (2022) <https://doi.org/10.1038/s41467-022-28791-x>
- [16] Kuschewski, F., Ribbeck, H.-G.v., Döring, J., Winnerl, S., Eng, L.M., Kehr, S.C.: Narrow-band near-field nanoscopy in the spectral range from 1.3 to 8.5 THz. *Applied Physics Letters* **108**(11), 113102 (2016) <https://doi.org/10.1063/1.4943793>
- [17] Jepsen, P.U., Cooke, D.G., Koch, M.: Terahertz spectroscopy and imaging – modern techniques and applications. *Laser & Photonics Reviews* **5**(1), 124–166 (2011) <https://doi.org/10.1002/lpor.201000011>
- [18] Moon, K., Park, H., Kim, J., Do, Y., Lee, S., Lee, G., Kang, H., Han, H.: Sub-surface nanoimaging by broadband terahertz pulse near-field microscopy. *Nano Letters* **15**(1), 549–552 (2015) <https://doi.org/10.1021/nl503998v>
- [19] Zhang, J., Chen, X., Mills, S., Ciavatti, T., Yao, Z., Mescall, R., Hu, H., Semenenko, V., Fei, Z., Li, H., Perebeinos, V., Tao, H., Dai, Q., Du, X., Liu, M.: Terahertz nanoimaging of graphene. *ACS Photonics* **5**(7), 2645–2651 (2018)

<https://doi.org/10.1021/acsp Photonics.8b00190>

- [20] Aghamiri, N.A., Huth, F., Huber, A.J., Fali, A., Hillenbrand, R., Abate, Y.: Hyperspectral time-domain terahertz nano-imaging. *Optics Express* **27**(17), 24231–24242 (2019) <https://doi.org/10.1364/OE.27.024231>
- [21] Kim, R.H.J., Huang, C., Luan, Y., Wang, L.-L., Liu, Z., Park, J.-M., Luo, L., Lozano, P.M., Gu, G., Turan, D., Yardimci, N.T., Jarrahi, M., Perakis, I.E., Fei, Z., Li, Q., Wang, J.: Terahertz nano-imaging of electronic strip heterogeneity in a dirac semimetal. *ACS Photonics* **8**(7), 1873–1880 (2021) <https://doi.org/10.1021/acsp Photonics.1c00216>
- [22] Plankl, M., Faria Junior, P.E., Mooshammer, F., Siday, T., Zizlsperger, M., Sandner, F., Schiegl, F., Maier, S., Huber, M.A., Gmitra, M., Fabian, J., Boland, J.L., Cocker, T.L., Huber, R.: Subcycle contact-free nanoscopy of ultrafast interlayer transport in atomically thin heterostructures. *Nature Photonics* (2021) <https://doi.org/10.1038/s41566-021-00813-y>
- [23] Jing, R., Shao, Y., Fei, Z., Lo, C.F.B., Vitalone, R.A., Ruta, F.L., Staunton, J., Zheng, W.J.C., McLeod, A.S., Sun, Z., Jiang, B.-y., Chen, X., Fogler, M.M., Millis, A.J., Liu, M., Cobden, D.H., Xu, X., Basov, D.N.: Terahertz response of monolayer and few-layer WTe₂ at the nanoscale. *Nature Communications* **12**(1), 5594 (2021) <https://doi.org/10.1038/s41467-021-23933-z>
- [24] Pizzuto, A., Chen, X., Hu, H., Dai, Q., Liu, M., Mittleman, D.M.: Anomalous contrast in broadband thz near-field imaging of gold microstructures. *Optics Express* **29**(10), 15190–15198 (2021) <https://doi.org/10.1364/OE.423528>
- [25] Yao, Z., Semenenko, V., Zhang, J., Mills, S., Zhao, X., Chen, X., Hu, H., Mescall, R., Ciavatti, T., March, S., Bank, S.R., Tao, T.H., Zhang, X., Perebeinos, V., Dai, Q., Du, X., Liu, M.: Photo-induced terahertz near-field dynamics of graphene/InAs heterostructures. *Optics Express* **27**(10), 13611–13623 (2019) <https://doi.org/10.1364/OE.27.013611>
- [26] Knoll, B., Keilmann, F.: Near-field probing of vibrational absorption for chemical microscopy. *Nature* **399**(6732), 134–137 (1999) <https://doi.org/10.1038/20154>
- [27] Cvitkovic, A., Ocelic, N., Hillenbrand, R.: Analytical model for quantitative prediction of material contrasts in scattering-type near-field optical microscopy. *Optics Express* **15**(14), 8550–8565 (2007) <https://doi.org/10.1364/OE.15.008550>
- [28] McLeod, A.S., Kelly, P., Goldflam, M.D., Gainsforth, Z., Westphal, A.J., Dominguez, G., Thiemens, M.H., Fogler, M.M., Basov, D.N.: Model for quantitative tip-enhanced spectroscopy and the extraction of nanoscale-resolved optical constants. *Physical Review B* **90**(8), 085136 (2014) <https://doi.org/10.1103/PhysRevB.90.085136>

- [29] Mester, L., Govyadinov, A.A., Hillenbrand, R.: High-fidelity nano-ftir spectroscopy by on-pixel normalization of signal harmonics. *Nanophotonics* **11**(2), 377–390 (2022) <https://doi.org/10.1515/nanoph-2021-0565>
- [30] Taubner, T., Hillenbrand, R., Keilmann, F.: Nanoscale polymer recognition by spectral signature in scattering infrared near-field microscopy. *Applied Physics Letters* **85**(21), 5064–5066 (2004) <https://doi.org/10.1063/1.1827334>
- [31] Brehm, M., Taubner, T., Hillenbrand, R., Keilmann, F.: Infrared spectroscopic mapping of single nanoparticles and viruses at nanoscale resolution. *Nano Letters* **6**(7), 1307–1310 (2006) <https://doi.org/10.1021/nl0610836>
- [32] Zhang, L.M., Andreev, G.O., Fei, Z., McLeod, A.S., Dominguez, G., Thiemens, M., Castro-Neto, A.H., Basov, D.N., Fogler, M.M.: Near-field spectroscopy of silicon dioxide thin films. *Physical Review B - Condensed Matter and Materials Physics* **85** (2012) <https://doi.org/10.1103/PhysRevB.85.075419>
- [33] Govyadinov, A.A., Mastel, S., Golmar, F., Chuvilin, A., Carney, P.S., Hillenbrand, R.: Recovery of permittivity and depth from near-field data as a step toward infrared nanotomography. *ACS Nano* **8**(7), 6911–6921 (2014) <https://doi.org/10.1021/nm5016314>
- [34] Wirth, K.G., Linnenbank, H., Steinle, T., Banszerus, L., Icking, E., Stampfer, C., Giessen, H., Taubner, T.: Tunable s-SNOM for nanoscale infrared optical measurement of electronic properties of bilayer graphene. *ACS Photonics* **8**(2), 418–423 (2021) <https://doi.org/10.1021/acsp Photonics.0c01442>
- [35] Fei, Z., Palomaki, T., Wu, S., Zhao, W., Cai, X., Sun, B., Nguyen, P., Finney, J., Xu, X., Cobden, D.H.: Edge conduction in monolayer WTe₂. *Nature Physics* **13**(7), 677–682 (2017) <https://doi.org/10.1038/nphys4091>
- [36] Kim, D.-S., Kwon, H., Nikitin, A.Y., Ahn, S., Martín-Moreno, L., García-Vidal, F.J., Ryu, S., Min, H., Kim, Z.H.: Stacking structures of few-layer graphene revealed by phase-sensitive infrared nanoscopy. *ACS Nano* **9**(7), 6765–6773 (2015) <https://doi.org/10.1021/acsnano.5b02813>
- [37] Conrad, G., Casper, C.B., Ritchie, E.T., Atkin, J.M.: Quantitative modeling of near-field interactions incorporating polaritonic and electrostatic effects. *Optics Express* **30**(7), 11619–11632 (2022) <https://doi.org/10.1364/OE.442305>
- [38] Mooshammer, F., Huber, M.A., Sandner, F., Plankl, M., Zizlsperger, M., Huber, R.: Quantifying nanoscale electromagnetic fields in near-field microscopy by Fourier demodulation analysis. *ACS Photonics* **7**(2), 344–351 (2020) <https://doi.org/10.1021/acsp Photonics.9b01533>
- [39] Mooshammer, F., Plankl, M., Siday, T., Zizlsperger, M., Sandner, F., Vitalone, R., Jing, R., Huber, M.A., Basov, D.N., Huber, R.: Quantitative terahertz emission

- nanoscopy with multiresonant near-field probes. *Optics Letters* **46**(15), 3572–3575 (2021) <https://doi.org/10.1364/OL.430400>
- [40] Maissen, C., Chen, S., Nikulina, E., Govyadinov, A., Hillenbrand, R.: Probes for ultrasensitive THz nanoscopy. *ACS Photonics* **6**(5), 1279–1288 (2019) <https://doi.org/10.1021/acsp Photonics.9b00324>
- [41] Rumyantsev, S., Liu, G., Stillman, W., Shur, M., Balandin, A.A.: Electrical and noise characteristics of graphene field-effect transistors: ambient effects, noise sources and physical mechanisms. *Journal of Physics: Condensed Matter* **22**(39), 395302 (2010) <https://doi.org/10.1088/0953-8984/22/39/395302>
- [42] Gammelgaard, L., Caridad, J.M., Cagliani, A., Mackenzie, D.M.A., Petersen, D.H., Booth, T.J., Bøggild, P.: Graphene transport properties upon exposure to PMMA processing and heat treatments. *2D Materials* **1**(3), 035005 (2014) <https://doi.org/10.1088/2053-1583/1/3/035005>
- [43] Lundeberg, M.B., Gao, Y., Asgari, R., Tan, C., Van Duppen, B., Autore, M., Alonso-González, P., Woessner, A., Watanabe, K., Taniguchi, T., Hillenbrand, R., Hone, J., Polini, M., Koppens, F.H.L.: Tuning quantum nonlocal effects in graphene plasmonics. *Science* **357**(6347), 187–191 (2017) <https://doi.org/10.1126/science.aan2735>
- [44] Carbotte, J.P., LeBlanc, J.P.F., Nicol, E.J.: Emergence of plasmaronic structure in the near-field optical response of graphene. *Physical Review B* **85**(20), 201411 (2012) <https://doi.org/10.1103/PhysRevB.85.201411>
- [45] Abergel, D.S.L., Apalkov, V., Berashevich, J., Ziegler, K., Chakraborty, T.: Properties of graphene: a theoretical perspective. *Advances in Physics* **59**(4), 261–482 (2010) <https://doi.org/10.1080/00018732.2010.487978>
- [46] Lovat, G., Hanson, G.W., Araneo, R., Burghignoli, P.: Semiclassical spatially dispersive intraband conductivity tensor and quantum capacitance of graphene. *Physical Review B* **87**(11), 115429 (2013) <https://doi.org/10.1103/PhysRevB.87.115429>
- [47] Jablan, M., Buljan, H., Soljačić, M.: Plasmonics in graphene at infrared frequencies. *Physical Review B* **80**(24), 245435 (2009) <https://doi.org/10.1103/PhysRevB.80.245435>
- [48] Casiraghi, C., Hartschuh, A., Lidorikis, E., Qian, H., Harutyunyan, H., Gokus, T., Novoselov, K.S., Ferrari, A.C.: Rayleigh imaging of graphene and graphene layers. *Nano Letters* **7**(9), 2711–2717 (2007) <https://doi.org/10.1021/nl071168m>
- [49] Jessen, B.S., Whelan, P.R., Mackenzie, D.M.A., Luo, B., Thomsen, J.D., Gammelgaard, L., Booth, T.J., Bøggild, P.: Quantitative optical mapping of two-dimensional materials. *Scientific Reports* **8**(1), 6381 (2018) <https://doi.org/10.1038/s41598-018-22700-4>

- [50] Liu, G., Rumyantsev, S., Shur, M.S., Balandin, A.A.: Origin of 1/f noise in graphene multilayers: Surface vs. volume. *Applied Physics Letters* **102**(9), 093111 (2013) <https://doi.org/10.1063/1.4794843>
- [51] Falkovsky, L.A.: Optical properties of graphene. *Journal of Physics: Conference Series* **129**(1), 012004 (2008) <https://doi.org/10.1088/1742-6596/129/1/012004>
- [52] Fei, Z., Andreev, G.O., Bao, W., Zhang, L.M., McLeod, A.S., Wang, C., Stewart, M.K., Zhao, Z., Dominguez, G., Thiemens, M., Fogler, M.M., Tauber, M.J., Castro-Neto, A.H., Lau, C.N., Keilmann, F., Basov, D.N.: Infrared nanoscopy of dirac plasmons at the graphene-sio2 interface. *Nano Letters* **11**(11), 4701–4705 (2011) <https://doi.org/10.1021/nl202362d>
- [53] Bhatnagar, P.L., Gross, E.P., Krook, M.: A model for collision processes in gases. i. small amplitude processes in charged and neutral one-component systems. *Physical Review* **94**(3), 511–525 (1954) <https://doi.org/10.1103/PhysRev.94.511>
- [54] Mermin, N.D.: Lindhard dielectric function in the relaxation-time approximation. *Physical Review B* **1**(5), 2362–2363 (1970) <https://doi.org/10.1103/physrevb.1.2362>
- [55] Ocelić, N.: Quantitative near-field phonon-polariton spectroscopy. Thesis, Technische Universität München (2007)
- [56] Hauer, B., Engelhardt, A.P., Taubner, T.: Quasi-analytical model for scattering infrared near-field microscopy on layered systems. *Optics Express* **20**(12), 13173–13188 (2012) <https://doi.org/10.1364/OE.20.013173>
- [57] Zhan, T., Shi, X., Dai, Y., Liu, X., Zi, J.: Transfer matrix method for optics in graphene layers. *J. Phys.: Condens. Matter* **25**(21), 215301 (2013) <https://doi.org/10.1088/0953-8984/25/21/215301>